

Investigating the Structural, Electronic, Optical, and Thermoelectric Properties of TiXO_3 ($\text{X} = \text{Nb}, \text{Ta}$) for Low-Cost Energy Applications

L. BENAHMEDI*, A. BESBES AND R. DJELTI

Technology and Solids Properties Laboratory, Faculty of Science and Technology, Mostaganem University, 27000 Mostaganem, Algeria

Received: & Accepted: 14.03.2025

Doi: [10.12693/APhysPolA.147.393](https://doi.org/10.12693/APhysPolA.147.393)

*e-mail: lakhdar.benahmedi@gmail.com

This study explores the structural, electronic, elastic, optical, and thermoelectric properties of two novel oxide perovskites, TiNbO_3 and TiTaO_3 , using density functional theory with the generalized gradient approximation and modified Becke–Johnson potential to accurately capture exchange–correlation effects. Our analysis confirms the thermodynamic stability of both compounds through assessments of cohesive energy, formation enthalpy, and phonon dispersion, indicating their cubic and dynamic stability. The band structure reveals that TiNbO_3 has a direct band gap of 0.17 eV, while TiTaO_3 exhibits a wider gap of 1.52 eV, confirming their semiconductor behavior. Elastic property calculations indicate that TiNbO_3 is brittle and TiTaO_3 is more ductile, with both materials demonstrating elastic anisotropy and a mix of metallic and covalent bonding. The density of states analysis highlights significant contributions from Ti, O, and Nb/Ta in the valence and conduction bands, emphasizing their potential in optoelectronic applications. Optical analyses further reveal high refractive indices and favorable dielectric properties, supporting their use in devices. Additionally, thermoelectric evaluations show a κ/σ ratio on the order of 10^{-5} , indicating low thermal conductivity alongside significant electrical conductivity. Notably, TiTaO_3 demonstrates substantial power factor values, positioning it as a promising candidate for thermal applications and energy conversion systems. Overall, this comprehensive investigation underscores the potential of TiNbO_3 and TiTaO_3 for advanced technological applications.

topics: oxide perovskites, density functional theory (DFT) calculations, band gap, thermoelectric properties

1. Introduction

The ongoing pursuit of sustainable energy solutions and efficient energy management is critical in addressing global challenges such as fossil fuel depletion and climate change [1]. As the world seeks alternatives to fossil fuels, energy storage technologies have become pivotal [2]. These technologies enable the capture and utilization of energy generated at various times, effectively addressing the intermittent nature of renewable energy sources and optimizing energy use in modern society [3]. Effective energy management supports not only industrial processes but also the performance of a wide range of electronic and electrical devices. In this context, dielectric materials and their associated technologies are essential, as they store and deliver energy rapidly, making them crucial for applications in hybrid electric vehicles, portable electronic devices, and pulse power systems [4–6].

Perovskite materials have emerged as promising candidates for addressing the global energy challenges of fossil fuel depletion and climate change [7]. The perovskite structure, characterized by its versatile ABX_3 composition, allows for incorporating a wide range of cations [8]. This adaptability results in materials with diverse and tunable properties, making perovskites highly suitable for various applications, including energy storage and conversion technologies [9, 10]. Their inherent stability, combined with unique electronic, magnetic, and optical properties, positions them as key materials in developing advanced technologies aimed at sustainable energy solutions [11–13]. Among the different classes of perovskites, oxide perovskites such as barium titanate (BaTiO_3) and strontium ruthenate (SrRuO_3) stand out due to their stability and functional versatility. These materials are integral to various applications, from capacitors and actuators to catalysts and photovoltaic systems. Their capacity to facilitate chemical reactions and absorb light makes them

indispensable in both energy production and environmental technologies. The robust performance of oxide perovskites in various industrial applications underscores their importance in advancing energy efficiency and sustainability [14–18]. In turn, halide perovskites, denoted by the formula ABX_3 , where 'X' is a halogen, have gained significant attention for their remarkable optoelectronic properties [19]. A notable example is methylammonium lead iodide ($MAPbI_3$), which has achieved high efficiency in solar cells and light-emitting diodes (LEDs). The low cost and ease of fabrication associated with halide perovskites further enhance their potential for renewable energy technologies. Their ability to efficiently convert light into electrical energy highlights their role in the ongoing quest for sustainable energy solutions [20, 21].

Among the various perovskite types, thallium-based perovskites offer intriguing possibilities due to thallium's high atomic number and variable oxidation states. These features can introduce unique characteristics into the perovskite lattice, potentially enhancing performance in applications such as thermoelectrics and catalysis [22]. The exploration of thallium oxide perovskites is of particular interest as they may provide new pathways for improving energy efficiency and developing innovative technologies. By leveraging the unique properties of thallium, researchers can unlock new opportunities for advancing energy-related applications and technologies [23].

Research on thallium-based perovskites has demonstrated their broad potential in fields such as optoelectronics, photovoltaics, and radiation detection. Yanagida and colleagues explored several Tl-based crystalline scintillators, including Tl_2ZrCl_6 [24], $TlXCl_3$ ($X = Mg, Cd, \text{ and } Ba$) [24], noting that Tl_2ZrCl_6 achieved the highest resolution of 5.6% at 662 keV [25, 26]. Zaman et al. [27] conducted an *ab initio* study of Tl-based chloroperovskites, specifically $TlXCl_3$ ($X = Ca \text{ and } Cd$), and emphasized the key role of thallium atoms in scintillation applications. Beck and colleagues' work [28] on synthesizing the thallium perovskite $TlPbCl_3$ found it promising for use in photovoltaic devices. Singh [29] examined the electronic structures of $TlGeI_3$, $TlSnI_3$, and $TlPbI_3$, identifying $TlPbI_3$ as a potential low-band-gap scintillator [29]. Sharma et al. [30] focused on chemical shifts in polycrystalline halides, such as ABX_3 ($A = Cs, Tl; B = Pb; X = Br, I$), using nuclear magnetic resonance (NMR) spectroscopy. Yadav et al. [31] explored the suitability of $TlPbX_3$ ($X = Cl, Br, I$) compounds for optoelectronics and renewable energy applications. Ayub and colleagues' research [32] highlighted the mechanical stability of cubic $TlXF_3$ ($X = Be, Sr$) compounds, indicating their potential in energy storage. Hany et al. [33] studied the electrical and optical properties of $TlPbI_3$ for gamma radiation detection, while Yousefzadeh and colleagues [34] developed $TlSnI_3/g-C_3N_4$ nanocomposites, which

showed promise for organic dye degradation. Mitro and colleagues' work [35] on $TlPbX_3$ ($X = Cl, Br$) under low pressure confirmed the semiconducting properties of these compounds, and Jin et al. [36] used density functional theory (DFT) to investigate $TlSnX_3$ ($X = Cl, Br, I$), revealing that the Rashba effect contributes to their semiconductor potential. Yang et al. [37] emphasized the utility of $TlPbI_3$ in producing radiation detectors for medical imaging, national security, astrophysics, and industrial monitoring. Lastly, Wakil Hasan and colleagues [38] provided a comprehensive investigation of $TlBO_3$ ($B = Cr, Mn$) perovskites, focusing on their structural, mechanical, elastic, electronic, optical, and thermodynamic properties using DFT calculations. Their study showed that both $TlCrO_3$ and $TlMnO_3$ exhibit good mechanical stability and ductility, as indicated by the fulfillment of Born criteria and favorable elastic moduli. The optical properties of these materials were particularly noteworthy, with potential applications in waveguides, ultralarge integration of circuits, microelectronics, and solar cells. The study highlighted that $TlCrO_3$ and $TlMnO_3$ demonstrate better absorption characteristics with spin configurations, suggesting their utility in advanced applications [38].

Despite these promising findings, a comprehensive theoretical understanding of thallium oxide perovskites remains underexplored. To address this, our study employs DFT to conduct an in-depth analysis of $TlXO_3$ ($X = Nb, Ta$) perovskites. Our goal is to investigate their structural, electronic, elastic, optical, and thermoelectric properties, providing a robust theoretical framework that will support future experimental research. By offering detailed insights into these materials, we aim to aid in their development and application in advanced technologies. Our theoretical work is intended to build on existing research and provide valuable data that can guide experimental efforts. We hope that our findings will facilitate the practical exploration of thallium oxide perovskites and contribute to their integration into cutting-edge technologies, ultimately supporting the broader goals of sustainable energy and efficient resource management.

2. Computational method

In this study, we employed first-principles calculations to investigate the structural, electronic, optical, and thermoelectric properties of thallium oxide-based perovskites $TlXO_3$ ($X = Nb, Ta$), crystallizing in the cubic $Pm-3m$ space group (no. 221). These calculations were performed using the full-potential linearized augmented plane wave (FP-LAPW) method [39], as implemented in the WIEN2k code [40], which is grounded in density functional theory (DFT) [41]. The exchange–correlation potential was treated using

the generalized gradient approximation (GGA) as developed by Perdew, Burke, and Ernzerhof (PBE functional) [42, 43], providing reliable results for the ground-state properties. In addition, the modified Becke–Johnson (TB-mBJ) potential was employed to improve the accuracy of the calculated electronic band gaps [44], offering a more realistic prediction of the materials’ optoelectronic behavior. The electronic configurations of the atoms involved are explicitly considered, with Nb: $[\text{Kr}]4d^45s^1$, Ta: $[\text{Xe}]4f^{14}5d^{10}6s^2$, Tl: $[\text{Xe}]4f^{14}5d^{10}6s^26p^1$, and O: $[\text{He}]2s^2p^4$. These configurations help determine the valence electrons that are directly involved in bonding and affect the electronic properties of the compounds. To optimize the lattice parameters, we set the muffin-tin radius (RMT) values to 1.92, 2.50, and 1.74 a.u. for Nb/Ta, Tl, and O atoms, respectively. These values were reduced by 5% to ensure a proper description of the interactions near the atomic spheres. Within the atomic spheres, the crystal potential and electronic wavefunctions were expanded using a maximum angular momentum cutoff of $l_{\text{max}} = 10$, and the plane-wave cutoff parameter $R_{\text{mt}} \times k_{\text{max}}$ was set to 7. The wave vector was extended up to $G_{\text{max}} = 12$ in the interstitial region to ensure high accuracy of these calculations. For geometric optimization, we used a $12 \times 12 \times 12$ k -point mesh, ensuring adequate convergence for the structural properties. For the calculation of the density of states (DOS), a denser $18 \times 18 \times 18$ k -point mesh was employed. The energy convergence criterion between successive iterations was set to 0.0001 Ry, and forces acting on the atoms were minimized to 1 mRy/Bohr. To analyze the lattice dynamics, we used the Phonopy code [45], calculating the phonon dispersion curves using a $5 \times 5 \times 5$ supercell and a k -mesh of $5 \times 5 \times 5$. This allowed us to evaluate the dynamic stability of the perovskite structures. The optical properties were determined from the complex dielectric function [46], which allowed us to derive the optical constants, including refractive indices, absorption coefficients, and reflectivity. These optical properties provide insights into the material’s suitability for applications such as photovoltaics and optoelectronic devices. To investigate the thermoelectric properties, we used the semi-classical Boltzmann transport theory as implemented in the BoltzTraP code [47]. A fine k -point grid of $46 \times 46 \times 46$ was applied to compute the thermoelectric response, including the Seebeck coefficient, electrical conductivity, and thermal conductivity.

3. Results and discussion

3.1. Structural properties

The tolerance factor (τ) is a critical parameter used to predict the structural stability and crystallization of perovskite compounds, particularly to

determine whether they will adopt a cubic, tetragonal, or orthorhombic phase. It is calculated using the bond lengths between the atoms in the perovskite structure and is given by [48]

$$\tau = 0.707 \frac{L_{\text{A-X}}}{L_{\text{B-X}}}. \quad (1)$$

In this case, $L_{\text{A-X}}$ refers to the bond length between the thallium atom (Tl) and the oxygen atom (O), while $L_{\text{B-X}}$ refers to the bond length between the B-site cation (Nb or Ta) and the oxygen atom (O). For the TlXO_3 ($X = \text{Nb, Ta}$) compounds, the bond lengths are $L_{\text{Tl-O}} = 3.36 \text{ \AA}$ and $L_{\text{B-O}} = 2.45 \text{ \AA}$. Using these bond lengths, the calculated tolerance factor is $\tau \approx 0.99$. This value, being close to 1, strongly supports the prediction that the compound crystallizes in a stable cubic phase. A tolerance factor near 1 typically indicates that the perovskite structure is stable in its ideal cubic form [48, 49]. In our exploration of the structural properties of TlNbO_3 and TlTaO_3 perovskites, we sought to evaluate their stability and potential application in advanced technologies, such as light-emitting diodes (LEDs), solid-state batteries, and solar panels. Using first-principles methods, we investigated key ground-state parameters to provide deeper insights into the stability and versatility of these materials for such applications [50].

The optimized geometries for TlNbO_3 and TlTaO_3 were determined by solving Murnaghan’s equation of state (EOS) [51]

$$E(V) = E_0 + \frac{B_0 V}{B'_0 (B'_0 - 1)} \left[\left(\frac{V_0}{V} \right)^{B'_0} - 1 \right], \quad (2)$$

where $E(V)$ represents the energy as a function of volume V , B_0 is bulk modulus, B'_0 is its pressure derivative, V_0 is the equilibrium volume, and E_0 is the equilibrium energy. These calculations unveiled that both perovskites adopt a cubic $Pm\text{-}3m$ structure. In this lattice, the thallium (Tl) atoms occupy the $1a$ (0, 0, 0) Wyckoff site, the B-cations (Nb and Ta) are located at the $1b$ (0.5, 0.5, 0.5) positions, and the oxygen (O) atoms are positioned at the $3c$ (0.5, 0.5, 0) Wyckoff site (see Fig. 1). Structural optimizations were carried out for nonmagnetic (NM), ferromagnetic (FM), and antiferromagnetic (AFM) configurations. As seen in Fig. 2a, b, the NM configuration was identified as the most stable, exhibiting the lowest ground-state energy among the three magnetic configurations. Table I (see also [52]) presents various key structural parameters, including the lattice constant (a_0), pressure derivative B'_0 , the ground-state energies E_{min} , the equilibrium volume V_0 , and energetic properties. The lattice constants (a_0) were optimized at 4.09 Å for TlNbO_3 and 4.08 Å for TlTaO_3 , which aligns well with previously reported theoretical data, confirming the accuracy of our results. In addition to the lattice parameters, the formation energy (ΔH_f) was calculated to assess the thermodynamic stability of these compounds. The formation

TABLE I

Lattice parameters, bulk moduli, equilibrium volume, and energetic properties of TiXO_3 perovskite in different magnetic states.

Material	State	a [Å]		B'_0	E_{\min} [Ry]	V_0 [(a.u.) ³]	ΔH_f [Ry]
		GGA	LDA				
TiNbO_3	NM	4.09	—	4.61	−48670.629055	462.2340	−0.457
	FM	4.09	—	4.61	−48670.629009	460.0457	
	AFM	4.09	—	4.61	−48670.628998	462.2378	
TiTaO_3	NM	4.08	3.85 [52]	4.90	−72281.949332	459.8744	−0.924
	FM	4.08	—	5.00	−72281.949327	459.8102	
	AFM	4.08	—	4.72	−72281.949219	459.9474	

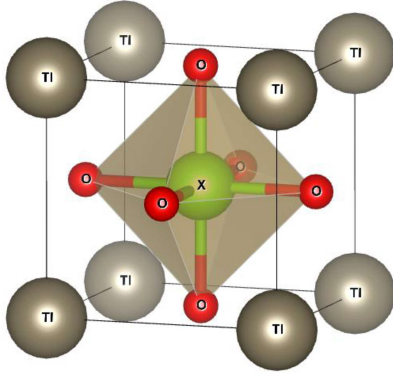


Fig. 1. Geometrically depicted cubic crystals of TiXO_3 ($X = \text{Nb}, \text{Ta}$) in the $Pm\text{-}3m$ space group.

energy is a crucial indicator of whether a material can be experimentally synthesized and is computed using [53]

$$\Delta H_f = E_{\text{TiXO}_3}^{\text{tot}} - (E_{\text{Ti}}^{\text{bulk}} + E_X^{\text{bulk}} + 3E_{\text{O}}^{\text{bulk}}), \quad (3)$$

where $E^{\text{tot}}(\text{TiXO}_3)$ represents the total energy of perovskite structure, and $E(\text{Ti})$, $E(X)$, and $E(\text{O})$ represent the energies of individual Ti, B-cation, and oxygen atoms, respectively. The formation energies for TiNbO_3 and TiTaO_3 were found to be -2.41 eV and -2.43 eV, respectively. The negative values of ΔH_f confirm the thermodynamic stability of these perovskites, indicating that they are energetically favorable for experimental synthesis. The slightly lower formation energy for TiTaO_3 suggests it may exhibit marginally higher stability than TiNbO_3 [54, 55].

3.2. Phonon dispersion

The phonon dispersion curves, density of states (DOS), and thermal phonon properties of the perovskite compounds TiNbO_3 and TiTaO_3 provide a comprehensive understanding of their lattice dynamics, vibrational behavior, and thermodynamic properties. Figure 3a–b reveals the vibrational

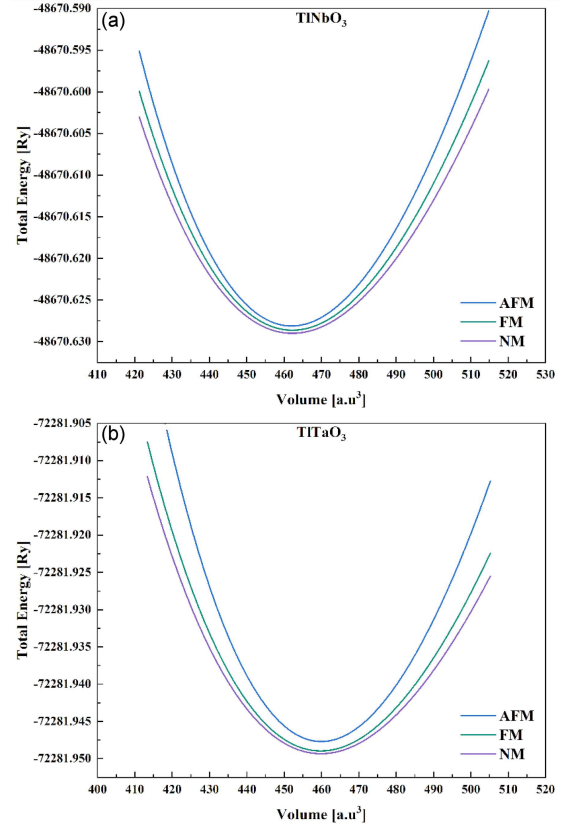


Fig. 2. Energy–volume optimization curves of TiXO_3 ($X = \text{Nb}, \text{Ta}$) in nonmagnetic, ferromagnetic, and antiferromagnetic phases.

characteristics of both compounds along high-symmetry directions ($\Gamma\text{-M-X-R-}\Gamma$) under the three phases: nonmagnetic (NM), ferromagnetic (FM), and antiferromagnetic (AFM). In this figure, the Γ point corresponds to the $\Gamma(\text{NM})$ for the nonmagnetic phase, and to $\Gamma(\text{A'FM}')$ for both the FM and AFM phases. In the FM phase, imaginary modes are observed, indicating the instability of this phase for both materials. In contrast, the NM and AFM phases display stable vibrational characteristics. The NM phase, characterized by the lowest ground energy, further supports its stability, making it the

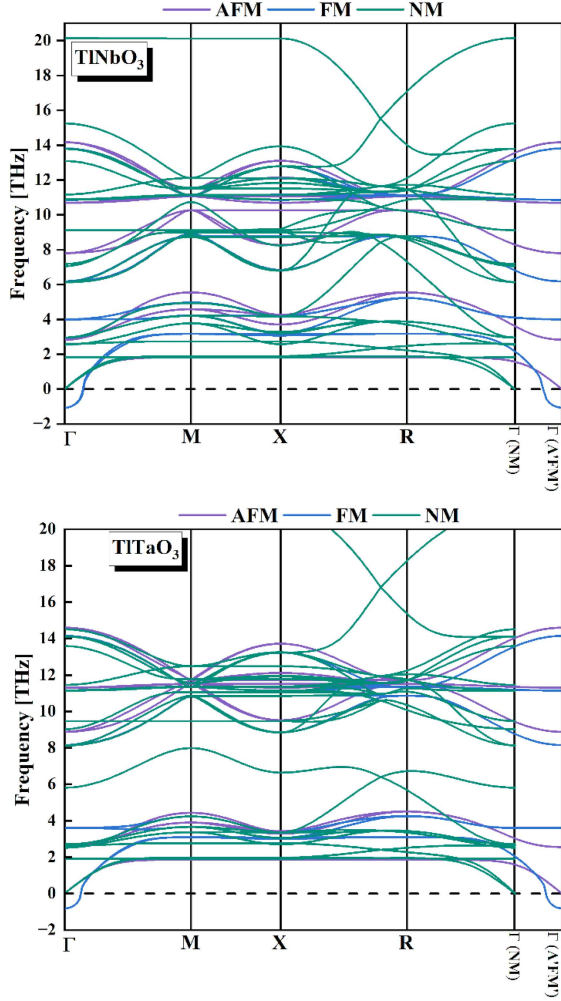


Fig. 3. Phonon dispersion curves for TiXO_3 ($X = \text{Nb, Ta}$) perovskites.

most stable phase for both compounds. This analysis underscores the dynamic stability of the NM and AFM phases, with the FM phase showing significant instabilities due to the appearance of imaginary phonon modes. In the nonmagnetic phase, each compound exhibits three acoustic branches and several optical branches, typical of perovskite structures. The acoustic modes, which originate from the Γ point at 0 THz, are crucial for thermal transport, while the optical branches appear at higher frequencies, primarily above 4 THz. The absence of imaginary (negative frequency) modes in both TiNbO_3 and TiTaO_3 confirms their dynamical stability, indicating no structural instabilities. The optical phonon branches in TiNbO_3 reach slightly higher frequencies (~ 15 THz) compared to TiTaO_3 , suggesting stronger bonding interactions in Nb–O bonds relative to Ta–O bonds. TiNbO_3 also shows more dispersive optical branches, indicating higher phonon group velocities, which could contribute to enhanced thermal transport compared to TiTaO_3 [56].

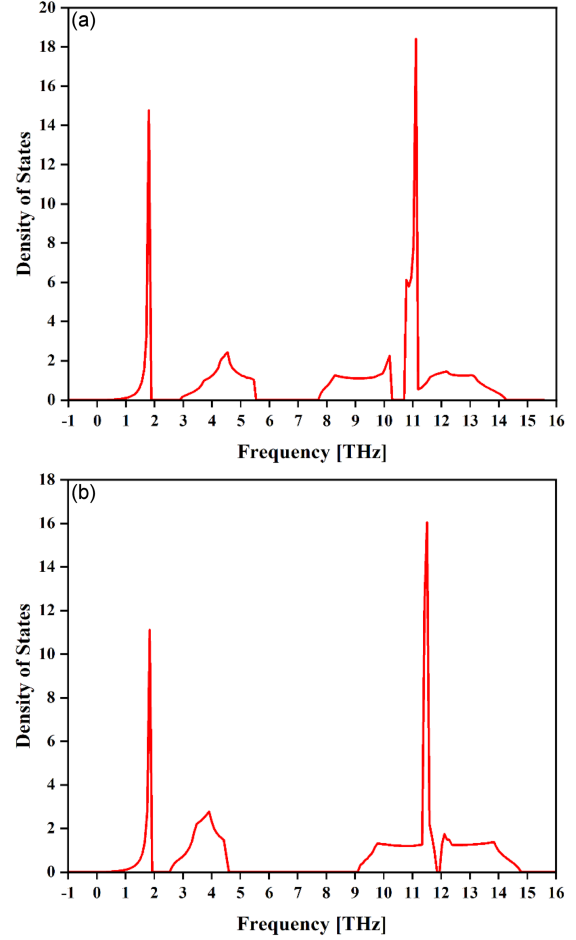


Fig. 4. Phonon density of states curves for (a) TiNbO_3 and (b) TiTaO_3 perovskites.

The phonon density of states (DOS) in Fig. 4a–b further clarifies the vibrational contributions of different atomic species. The low-frequency region (0–5 THz) is dominated by vibrations from the heavy Ti and O atoms, while the mid-frequency range (5–10 THz) corresponds to a mixture of oxygen $2p$ states and B-cation (Nb or Ta) vibrations. The high-frequency peaks above 10 THz are mainly associated with Nb $4d$ and Ta $5d$ states, indicating that the B-cation plays a crucial role in determining the phonon behavior. The DOS of TiNbO_3 shows a broader distribution in the mid-frequency range, implying stronger hybridization between Nb and O atoms, while TiTaO_3 exhibits a slightly sharper high-frequency peak, suggesting stiffer Ta–O bonds. These variations in the phonon DOS influence the thermal transport properties, as materials with broader DOS distributions often exhibit increased phonon scattering [57].

The phonon thermal properties curves shown in Fig. 5a–b illustrate the temperature dependence of Helmholtz free energy (F), entropy (S), heat capacity (C_V), and internal energy (E). The free energy decreases with increasing temperature

TABLE II

Band gaps of TiXO_3 calculated using GGA-PBE, TB-mBJ, LDA (local density approximation), and mBJ.

Material	Approximation				Band gap type
	GGA-PBE	TB-mBJ	LDA	mBJ LDA	
	this work		other works		
TiNbO_3	0.246	0.175	—	—	direct
TiTaO_3	0.832	1.18	0.55 [52]	1.22 [52]	direct

, reflecting the anharmonic nature of lattice vibrations, while the entropy increases, indicating enhanced disorder in the phonon system at higher temperatures [58]. The heat capacity (C_V) initially rises with temperature and eventually saturates, consistent with the Dulong–Petit limit, where all phonon modes are fully excited [59]. The internal energy follows a nearly linear trend with temperature, as expected from phonon contributions. The slightly higher entropy and internal energy values of TiNbO_3 suggest stronger phonon interactions and a higher density of vibrational states compared to TiTaO_3 . The heat capacity behavior also implies that TiNbO_3 may reach thermal equilibrium faster than TiTaO_3 , influencing its potential applications in thermal management and dielectric properties [60].

The combined phonon dispersion, DOS, and thermal phonon analyses indicate that TiNbO_3 exhibits stronger lattice interactions and higher phonon frequencies, suggesting superior thermal transport properties compared to TiTaO_3 . The absence of imaginary frequencies in both compounds confirms their dynamical stability, and the variations in phonon behavior between Nb- and Ta-based perovskites highlight the impact of B-site cation selection on vibrational and thermal characteristics.

3.3. Electronic properties

3.3.1. Band structure

Band structures are essential in determining the electronic properties, revealing how electrons behave in a material and the energy required to transition between states [61]. As shown in Fig. 6a–b, the band structure for TiNbO_3 and TiTaO_3 demonstrates a clear semiconductor behavior with a direct band gap located at the X point. For TiNbO_3 , the band gap calculated using the GGA-PBE functional is 0.246 eV, whereas TiTaO_3 shows a larger gap of 0.832 eV. These results are summarized in Table II (see also [52]). After applying the more advanced TB-mBJ method, which provides a more accurate prediction of band gaps, we observe a slight decrease in TiNbO_3 's gap to 0.175 eV, while TiTaO_3 's gap increases to 1.18 eV. Additionally, the local density approximation (LDA), another

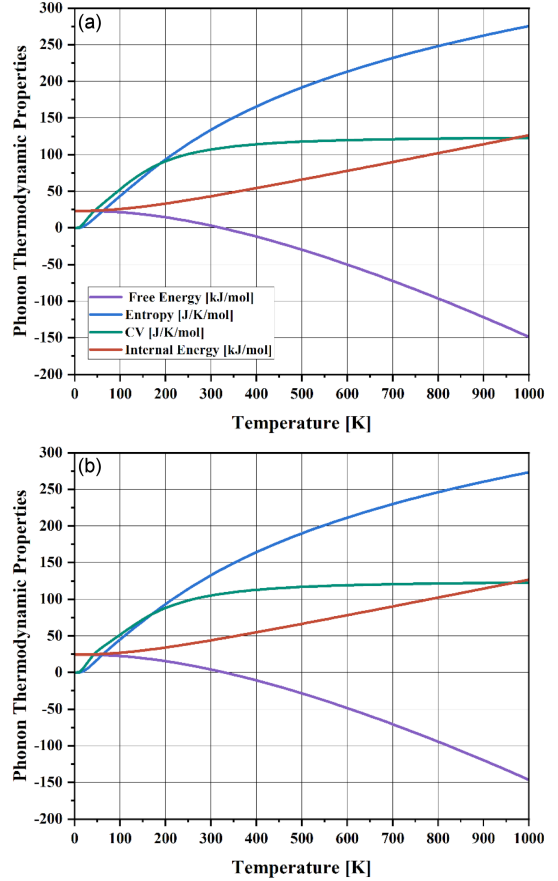


Fig. 5. Phonon thermal properties curves for (a) TiNbO_3 and (b) TiTaO_3 perovskites.

common method in density functional theory, predicts a band gap of 0.55 eV for TiTaO_3 (as reported in previous works [55]), which is lower than the TB-mBJ value but higher than GGA-PBE. For TiNbO_3 , LDA data is not available in the literature for comparison.

The refinement of these values with TB-mBJ suggests that TiNbO_3 , with its smaller band gap, might be well-suited for low-energy applications such as photodetectors, while the larger gap in TiTaO_3 indicates a potential for higher-energy applications, like ultraviolet (UV) detectors [62]. Both materials maintain a direct band gap at the X point, making them promising for efficient optical transitions in various optoelectronic devices.

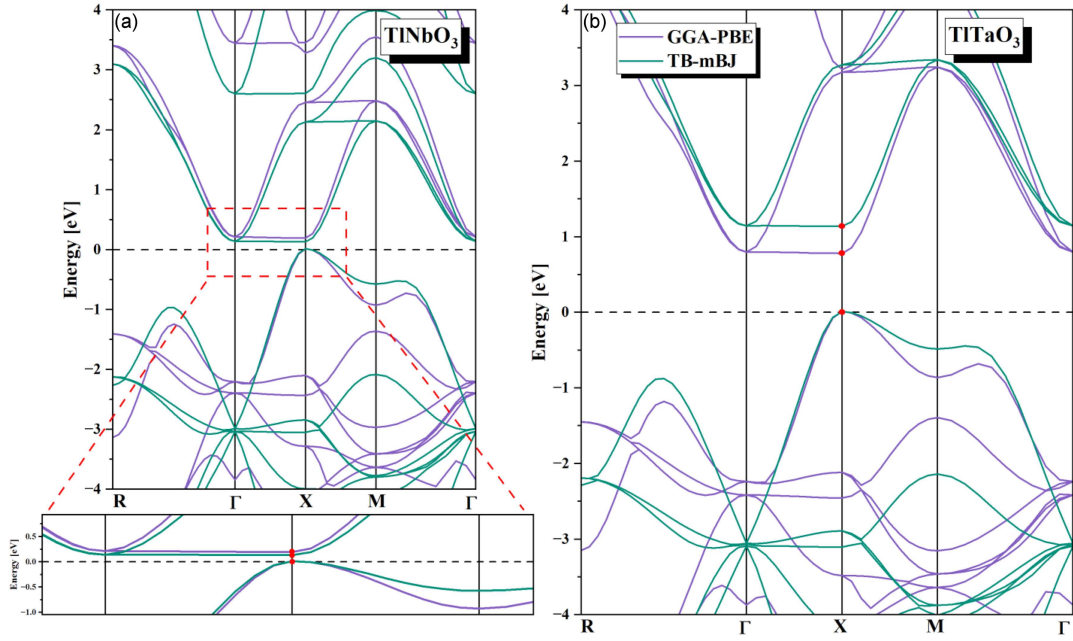


Fig. 6. Band structure of TIXO_3 ($X = \text{Nb}, \text{Ta}$) perovskites based on GGA-PBE and TB-mBJ predictions.

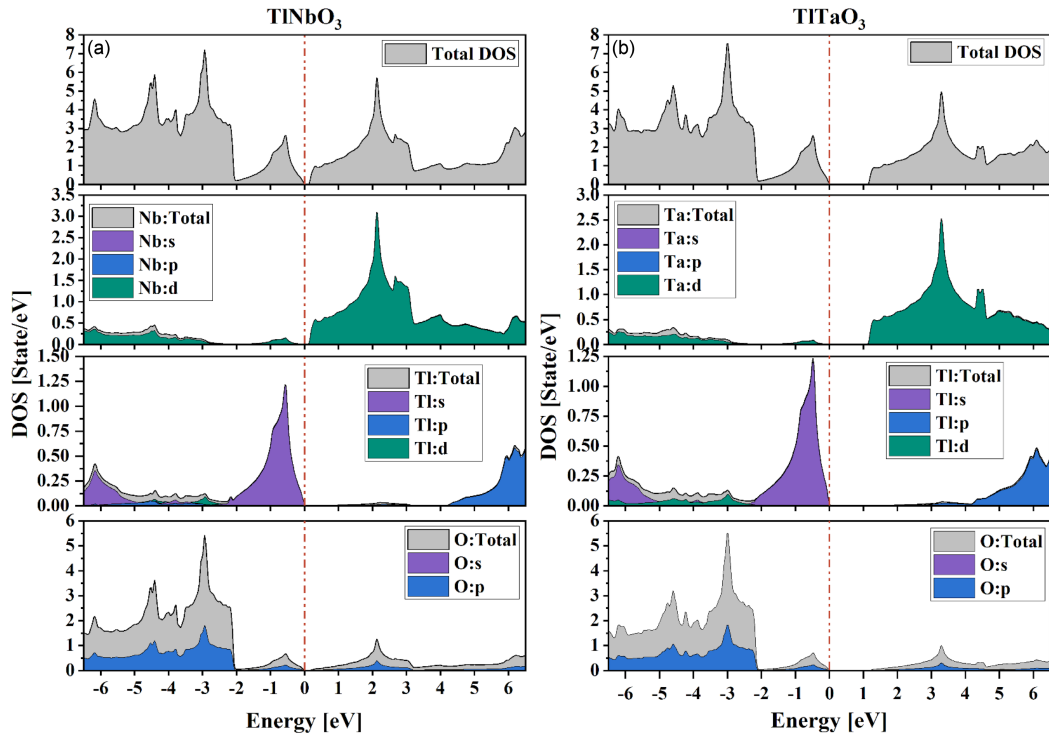


Fig. 7. Total and projected density of states for TIXO_3 ($X = \text{Nb}, \text{Ta}$) perovskite oxides.

3.3.2. Density of state

In our density of states (DOS) and partial density of states (PDOS) analysis for TIXO_3 ($X = \text{Nb}, \text{Ta}$) perovskite oxides, as plotted in Fig. 7a–b, we

investigated the energy range from -6.5 to 6.5 eV. The results clearly confirm the semiconducting nature of these compounds. The DOS and PDOS reveal distinct contributions from different atomic orbitals in both the valence and conduction bands. The valence band, in the negative energy range, is

primarily dominated by the $6s$ orbitals of the thallium (Tl) atom near the Fermi level, with minor contributions from the $2p$ orbitals of the oxygen (O) atom and the $4d$ orbitals of the B-cation (Nb) in TlNbO_3 or $5d$ orbitals in TlTaO_3 . The lower energy levels of the valence band (-2 to -6 eV) are mainly dominated by the $2p$ orbitals of the oxygen atoms, indicating strong bonding interactions within the lattice. In the conduction band, the positive energy range near the conduction band minimum is dominated by the $4d$ orbitals of Nb in TlNbO_3 or the $5d$ orbitals of Ta in TlTaO_3 , suggesting that the B-cation significantly contributes to the conduction properties of these materials. In the middle energy range (~ 3 eV), there is a noticeable interaction from the $2p$ orbitals of oxygen, indicating some hybridization between the oxygen and B-cation orbitals. At higher energy levels, there is a minor contribution from the $6p$ orbitals of the Tl atom, which might influence the higher energy conduction states. Our findings align well with those of other similarly studied compounds, such as TlGeX_3 ($X = \text{Cl, Br, and I}$), further confirming the robustness of our analysis [63].

3.4. Mechanical stability

In this part, we investigate the mechanical properties of TlNbO_3 and TlTaO_3 to confirm the stability of these compounds. Specifically, we examine the bulk modulus (B), shear modulus (G), Young's modulus (E), Poisson's ratio (ν), Cauchy pressure (C_p), anisotropic factor (A), and Pugh's ratio (B/G). These properties are calculated using

$$B = \frac{1}{3}(C_{11} + 2C_{12}), \quad (4)$$

$$G = \frac{C_{11} - C_{12}}{2}, \quad (5)$$

$$E = \frac{9BG}{3B + G}, \quad (6)$$

$$\nu = \frac{3B - 2G}{2(3B + G)}, \quad (7)$$

$$C_p = C_{12} - C_{44}, \quad (8)$$

$$A = \frac{C_{44}}{C_{11} - C_{12}}. \quad (9)$$

The equations (4)–(9) allow us to derive the parameters and assess the materials' stability and mechanical behavior [64], and the results are summarized in Table III.

The elastic constants indicate that both materials are stable under deformation, meeting the Born stability criteria [65]. For TlNbO_3 , $C_{11} - C_{12} = 254.60$ GPa, which is greater than zero, and $C_{11} + 2C_{12} = 542.550$ GPa, which is also positive.

TABLE III

Mechanical properties of TlXO_3 antiperovskites.

Property	TlNbO_3	TlTaO_3
C_{11} [GPa]	350.588	388.171
C_{12} [GPa]	95.981	9.691
C_{44} [GPa]	82.566	83.481
bulk modulus (B)	35.344	24.246
shear modulus (G)	43.993	35.640
Young's modulus (E)	56.783	29.973
Poisson's ratio (ν)	0.066	0.033
Cauchy pressure (C_p)	-8.985	-13.890
anisotropic factor (A)	0.169	0.243
Pugh's ratio (B/G)	0.803	0.679

This shows stability against deformation. Similarly, TlTaO_3 meets the criteria with $C_{11} - C_{12} = 378.480$ GPa and $C_{11} + 2C_{12} = 389.553$ GPa, confirming its stability. Both materials satisfy the conditions $C_{11} > 0$, $C_{44} > 0$, and $C_{12} < C_{11}$, indicating they are stable under various strains. The bulk modulus for TlNbO_3 is 180.85 GPa, which is relatively high and suggests that this compound has good resistance to uniform compression. In comparison, TlTaO_3 has a lower bulk modulus of 135.85 GPa, indicating that it is more compressible under applied stress. This reflects weaker resistance to volumetric deformation relative to TlNbO_3 [66]. The shear modulus for TlNbO_3 is $G = 100.46$ GPa, which is lower than for TlTaO_3 , i.e., $G = 125.78$ GPa. This suggests that TlTaO_3 has better resistance to shear deformation, making it harder and more resistant to shape changes under shear stress [67]. Young's modulus is higher for TlTaO_3 ($E = 288.36$ GPa) than for TlNbO_3 ($E = 254.30$ GPa). This indicates that TlTaO_3 is stiffer and more resistant to stretching under tensile stress. In contrast, TlNbO_3 — although still relatively stiff — is less stiff compared to TlTaO_3 [68]. The Poisson's ratio of TlNbO_3 is 0.266, while for TlTaO_3 it is 0.146. These values indicate that TlNbO_3 exhibits a greater volumetric response to axial stress than TlTaO_3 . The lower Poisson's ratio for TlTaO_3 suggests it has more covalent bonding, as compared to the metallic bonding suggested by TlNbO_3 's higher Poisson's ratio [69]. The Cauchy pressure for TlNbO_3 is positive at 13.41 GPa, which aligns with metallic bonding characteristics. In contrast, TlTaO_3 has a negative Cauchy pressure of -73.79 GPa, indicating a more covalent nature of bonding [70]. The anisotropic factor for TlNbO_3 is 0.649, which is higher than 0.441 for TlTaO_3 , suggesting that TlNbO_3 's mechanical properties are more directionally dependent [69]. Finally, Pugh's ratio is 1.80 for TlNbO_3 , indicating ductile behavior, whereas the ratio for TlTaO_3 of 1.08 suggests that it is more brittle. This confirms that TlNbO_3 is more ductile, while TlTaO_3 , with its lower Pugh's ratio, is more prone to brittleness [71].

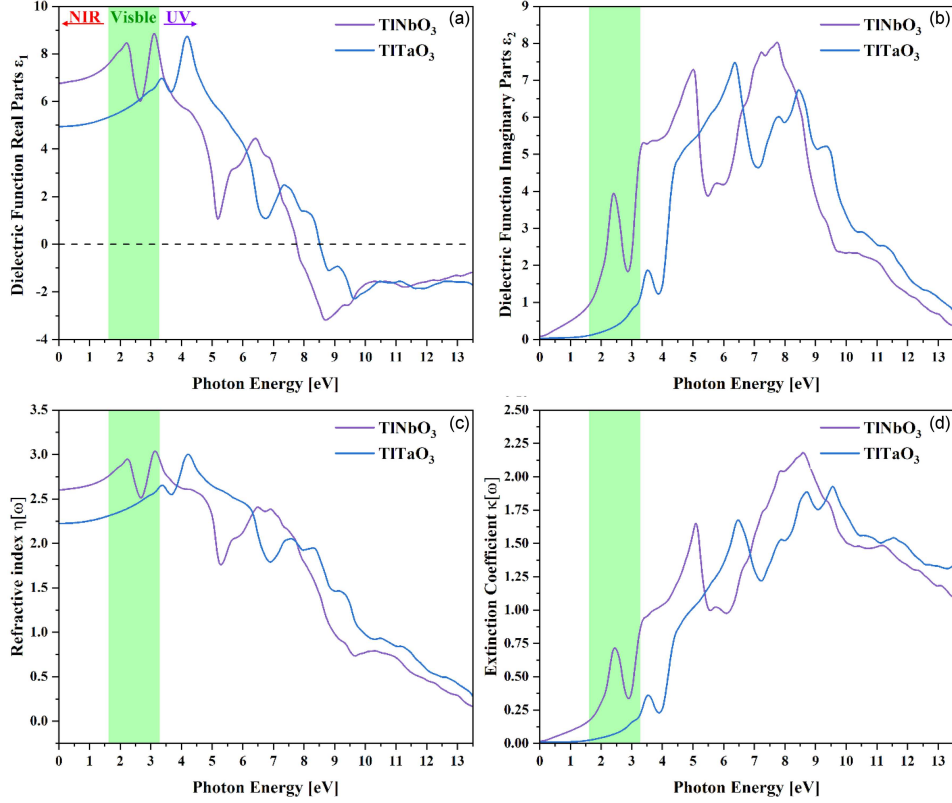


Fig. 8. (a) Real and (b) imaginary parts of the dielectric function, (c) refractive index, and (d) extinction coefficient for TiXO₃ (X = Nb, Ta) perovskite oxides.

3.5. Optical properties

In our study, the dielectric function, refractive index, extinction coefficient, absorption coefficient, energy loss, and reflectivity were calculated based on the equations outlined below

$$\varepsilon(\omega) = \varepsilon_1(\omega) + i\varepsilon_2(\omega), \quad (10)$$

$$\varepsilon_1(\omega) = 1 + \frac{2}{\pi} P \int_0^{\infty} d\omega' \frac{\varepsilon_2(\omega') \omega'}{\omega^2 - \omega'^2}, \quad (11)$$

$$\varepsilon_2(\omega) = \frac{e^2 h'}{\pi m^2 \omega^2} \sum_{V,C} \int_{\text{BZ}} d^3K |M_{V,C}(K)|^2 \times \delta(\omega_{C,V}(K) - \omega), \quad (12)$$

$$\eta(\omega) = \left[\frac{\varepsilon_1(\omega)}{2} + \frac{\sqrt{\varepsilon_1^2(\omega) + \varepsilon_2^2(\omega)}}{2} \right]^{\frac{1}{2}}, \quad (13)$$

$$k(\omega) = \left[-\frac{\varepsilon_1(\omega)}{2} + \frac{\sqrt{\varepsilon_1^2(\omega) + \varepsilon_2^2(\omega)}}{2} \right]^{\frac{1}{2}}, \quad (14)$$

$$R = \left| \frac{n_1 - n_2}{n_1 + n_2} \right|^2, \quad (15)$$

$$L(\omega) = \frac{\varepsilon_2(\omega)}{\varepsilon_1^2(\omega) + \varepsilon_2^2(\omega)}, \quad (16)$$

$$\alpha(\omega) = \frac{2\omega}{c} k(\omega), \quad (17)$$

where c is the speed of light in vacuum. The equations (10)–(17) provide the mathematical framework to derive the optical properties, enabling us to analyze the electronic transitions and interaction of electromagnetic waves with the material [72].

The results are presented in Figs. 7a–c and 8a–d. In Fig. 8a, the real part of the dielectric function, ε_1 , reveals significant insights. For TiNbO₃, the static dielectric constant, $\varepsilon_1(0)$, is 6.77, highlighting its strong polarizability at low frequencies. We observed the first peak in the visible range at 2.20 eV with a value of 8.46, followed by the highest peak at 3.09 eV with a value of 8.86. These peaks suggest notable optical activity and electronic transitions in the visible spectrum. In contrast, TiTaO₃ exhibits a lower static dielectric constant of 4.95, with a stronger response in the ultraviolet (UV) region. Its highest peak occurs at 4.14 eV with a value of 8.75, indicating that its primary optical transitions occur at higher energies. Furthermore, ε_1 becomes negative at 7.77 eV for TiNbO₃ and 8.52 eV for TiTaO₃, signifying a transition to metallic behavior beyond these energy thresholds.

The imaginary part of the dielectric function, ε_2 , depicted in Fig. 8b, complements these observations. TiNbO₃ shows its first peak in the visible range at 2.40 eV with a value of 3.95, while its highest peak occurs in the UV range at 7.76 eV with a value of 8.01. On the other hand, TiTaO₃

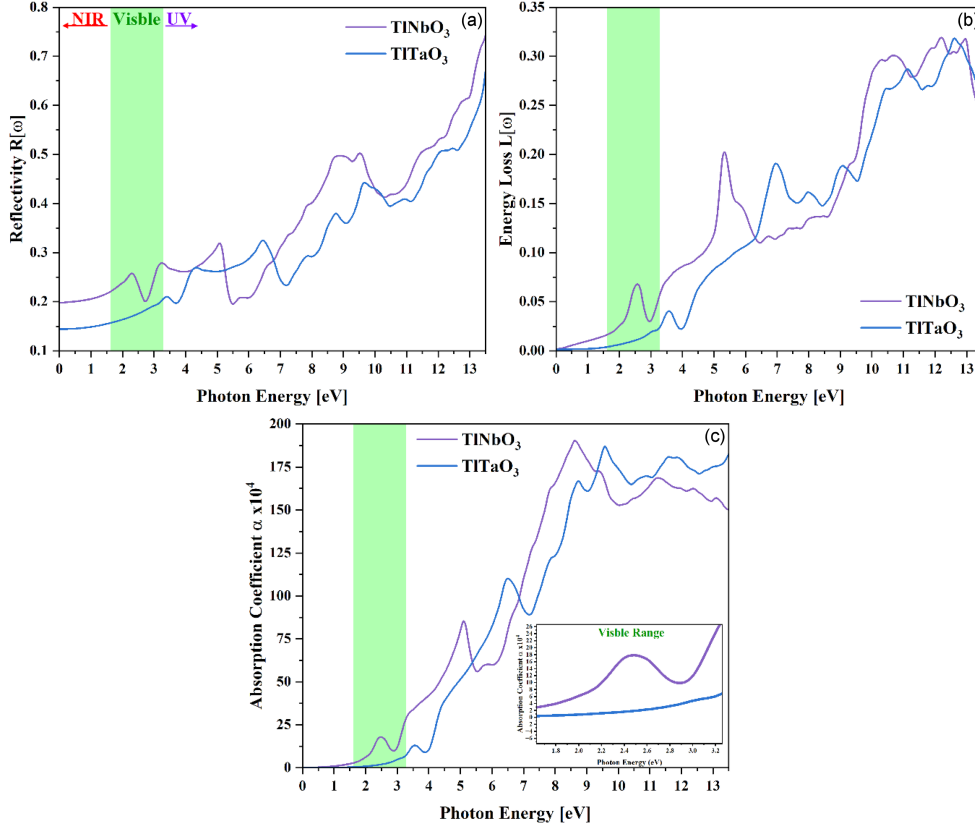


Fig. 9. (a) Reflectivity, (b) energy loss function, and (c) absorption coefficient for TiXO₃ (X = Nb, Ta) perovskite oxides.

has its first peak in the UV region at 3.51 eV with a value of 1.85, with the highest peak at 6.34 eV at a value of 7.50. These peaks correspond to interband electronic transitions and indicate strong optical absorption, particularly in the UV range.

Similarly, the refractive index $\eta(\omega)$, shown in Fig. 8c, follows the trend of ε_1 . TiNbO₃ shows two peaks in the visible range, with values of 2.94 and 3.04, emphasizing its optical response to visible light. TiTaO₃, however, shows its peaks in the UV region with values of 2.65 and 3.01, making it more suitable for UV applications. The extinction coefficient $\kappa(\omega)$ in Fig. 8d mirrors ε_2 closely. For TiNbO₃, the first peak is observed in the visible range at 2.42 eV with a value of 0.71, while the highest peak occurs in the UV range at 8.59 eV with a value of 2.18. TiTaO₃ shows its first peak in the UV region at 3.54 eV with a value of 0.35, and the highest peak at 9.56 eV with a value of 1.92.

The reflectivity $R(\omega)$, shown in Fig. 9a, demonstrates that TiNbO₃ has a static reflectivity $R(0)$ of 0.19, while TiTaO₃ exhibits a slightly lower $R(0)$ of 0.14. Across the energy range from 0 to 13.5 eV, the highest reflectivity for both materials does not exceed 0.75. In the visible range, the reflectivity remains below 0.3 for both compounds, indicating moderate reflectance, which is more pronounced in the UV region. This suggests that these materials

may absorb more light than they reflect in the visible spectrum, a desirable feature for optoelectronic applications.

The energy loss function $E(\omega)$, presented in Fig. 9b, shows relatively low values for both compounds in the visible range, not exceeding 0.06. This behavior suggests minimal energy dissipation due to plasmonic or electronic transitions at visible wavelengths. In the UV range, the energy loss increases, reaching a maximum of 0.31 for both materials, indicating a stronger interaction between incident photons and the electron gas at higher energies.

The absorption coefficient $\alpha(\omega)$, plotted in Fig. 9c, reveals distinct behavior for TiNbO₃ and TiTaO₃. In the near-infrared (NIR) range, TiNbO₃ shows a low absorption coefficient, while TiTaO₃ exhibits almost zero absorption in this range. In the visible range, TiNbO₃ presents its first absorption peak at 2.43 eV with a value of 18.33, followed by a decrease and then reaching its highest visible-range peak of 28.35 at 3.25 eV. TiTaO₃, however, shows no significant peak in the visible range, with a maximum absorption value of 6.90 at 3.25 eV. In the UV range, TiNbO₃ reaches its highest absorption peak of 190.60 at 8.60 eV, indicating strong photon absorption at high energies. TiTaO₃ shows its first absorption peak in the UV region at 3.56 eV with a value of 13.18, and its highest peak

at 9.56 eV with a value of 186.93. These results highlight that TiNbO₃ is more active in both the visible and UV ranges, while TiTaO₃ primarily exhibits strong absorption in the UV region.

The reflectivity, energy loss, and absorption coefficient analyses suggest that TiNbO₃ is more suited for applications that require strong absorption across the visible and UV ranges. At the same time, TiTaO₃ is better tailored for UV-specific applications. The optical characteristics of both materials indicate their potential for diverse optoelectronic and photonic applications.

3.6. Thermoelectric properties

The thermoelectric properties of the materials under investigation allow us to evaluate their potential for energy conversion applications by examining key parameters like the Seebeck coefficient (S), electrical conductivity (σ), thermal conductivity (κ), and the overall figure of merit (ZT). In this context, thermal properties were calculated using [73]

$$ZT = \frac{\sigma S^2 T}{\kappa}, \quad (18)$$

$$PF = S^2 \frac{\sigma}{\kappa}, \quad (19)$$

$$\sigma_{\alpha\beta}(T, \mu) = \frac{1}{V} \int d\varepsilon \sigma_{\alpha\beta}(\varepsilon) \left[-\frac{\partial f(T, \varepsilon, \mu)}{\partial \varepsilon} \right], \quad (20)$$

$$S_{\alpha\beta}(T, \mu) = \frac{1}{eTV \sigma_{\alpha\beta}(T, \mu)} \times \int d\varepsilon \sigma_{\alpha\beta}(\varepsilon) (\varepsilon - \mu) \left[-\frac{\partial f(T, \varepsilon, \mu)}{\partial \varepsilon} \right], \quad (21)$$

$$\kappa_{\alpha\beta}^e(T, \mu) = \frac{1}{e^2 T V} \times \int d\varepsilon \sigma_{\alpha\beta}(\varepsilon) (\varepsilon - \mu)^2 \left[-\frac{\partial f(T, \varepsilon, \mu)}{\partial \varepsilon} \right], \quad (22)$$

$$\sigma_{\alpha\beta}(\varepsilon) = \frac{1}{N} \sum_{i,k} \sigma_{\alpha\beta}(i, k) \frac{\delta(\varepsilon - \varepsilon_{i,k})}{\delta(\varepsilon)} = \frac{e^2}{N} \sum_{i,k} \tau_{i,k} \nu_{\alpha}(i, k) \nu_{\beta}(i, k) \frac{\delta(\varepsilon - \varepsilon_{i,k})}{\delta(\varepsilon)}. \quad (23)$$

Thermal properties, followed by the power factor (PF), are shown in Fig. 10a–e.

Figure 10a illustrates the variation of the Seebeck coefficient as a function of temperature for TiTaO₃ and TiNbO₃. The Seebeck coefficient represents the voltage generated in response to a temperature gradient across the material. Positive values of this coefficient indicate that the material is a p-type semiconductor, where holes act as the primary charge carriers. Based on the plotted data, both TiTaO₃ and TiNbO₃ exhibit positive Seebeck coefficients throughout the temperature range,

confirming their p-type behavior. At lower temperatures, the Seebeck coefficient values for both materials are relatively small but gradually increase as the temperature rises. This trend suggests an enhancement in thermoelectric performance with increasing temperature. TiTaO₃, in particular, shows consistently higher Seebeck values compared to TiNbO₃, indicating that TiTaO₃ may have better potential for thermoelectric applications at elevated temperatures. At 300 K, TiTaO₃ has a Seebeck coefficient of $\approx 2.13 \mu\text{V/K}$, while for TiNbO₃ it shows a slightly lower value of $1.87 \mu\text{V/K}$. As the temperature approaches 1200 K, the Seebeck coefficient of TiTaO₃ continues to rise, whereas TiNbO₃ exhibits a gradual decrease beyond a certain point, showing a different thermoelectric behavior at high temperatures. This indicates that TiNbO₃ might not perform as efficiently at very high temperatures, while TiTaO₃ maintains a strong performance throughout the examined range. The positive values of the Seebeck coefficient across the temperature range confirm that both materials exhibit p-type semiconductor characteristics, making them suitable candidates for thermoelectric applications where hole carriers dominate. Further analysis will explore their electrical conductivity, thermal conductivity, power factor, and figure of merit to provide a complete picture of their thermoelectric potential [74].

Electrical conductivity (σ) is critical for evaluating how well a material can conduct electric current, which directly influences thermoelectric efficiency. The data reveal the temperature dependence of electrical conductivity for TiTaO₃ and TiNbO₃. As shown in Fig. 10b, both materials exhibit a clear increase in electrical conductivity with rising temperature. This trend indicates enhanced charge carrier mobility and concentration as thermal energy increases. At low temperatures, TiTaO₃ and TiNbO₃ show relatively lower conductivity values, but as the temperature approaches 1200 K, both materials exhibit significant increases. For instance, at 300 K, TiTaO₃ has an electrical conductivity of approximately $2.86 \times 10^{18} (\Omega \text{ cm s})^{-1}$, while TiNbO₃ shows a slightly lower value of about $2.73 \times 10^{18} (\Omega \text{ cm s})^{-1}$. By 1200 K, TiTaO₃ reaches an impressive conductivity of about $1.68 \times 10^{19} (\Omega \text{ cm s})^{-1}$, and TiNbO₃ of $\approx 2.78 \times 10^{19} (\Omega \text{ cm s})^{-1}$. The higher conductivity of TiNbO₃ at elevated temperatures suggests that it may have a larger number of charge carriers or better charge transport characteristics compared to TiTaO₃ under those conditions. However, both materials demonstrate strong potential for thermoelectric applications due to their conductivity increasing with temperature, which is beneficial for efficient energy conversion [75].

Thermal conductivity (κ) quantifies a material's ability to conduct heat and is an important parameter in assessing thermoelectric performance. The data indicate how thermal conductivity

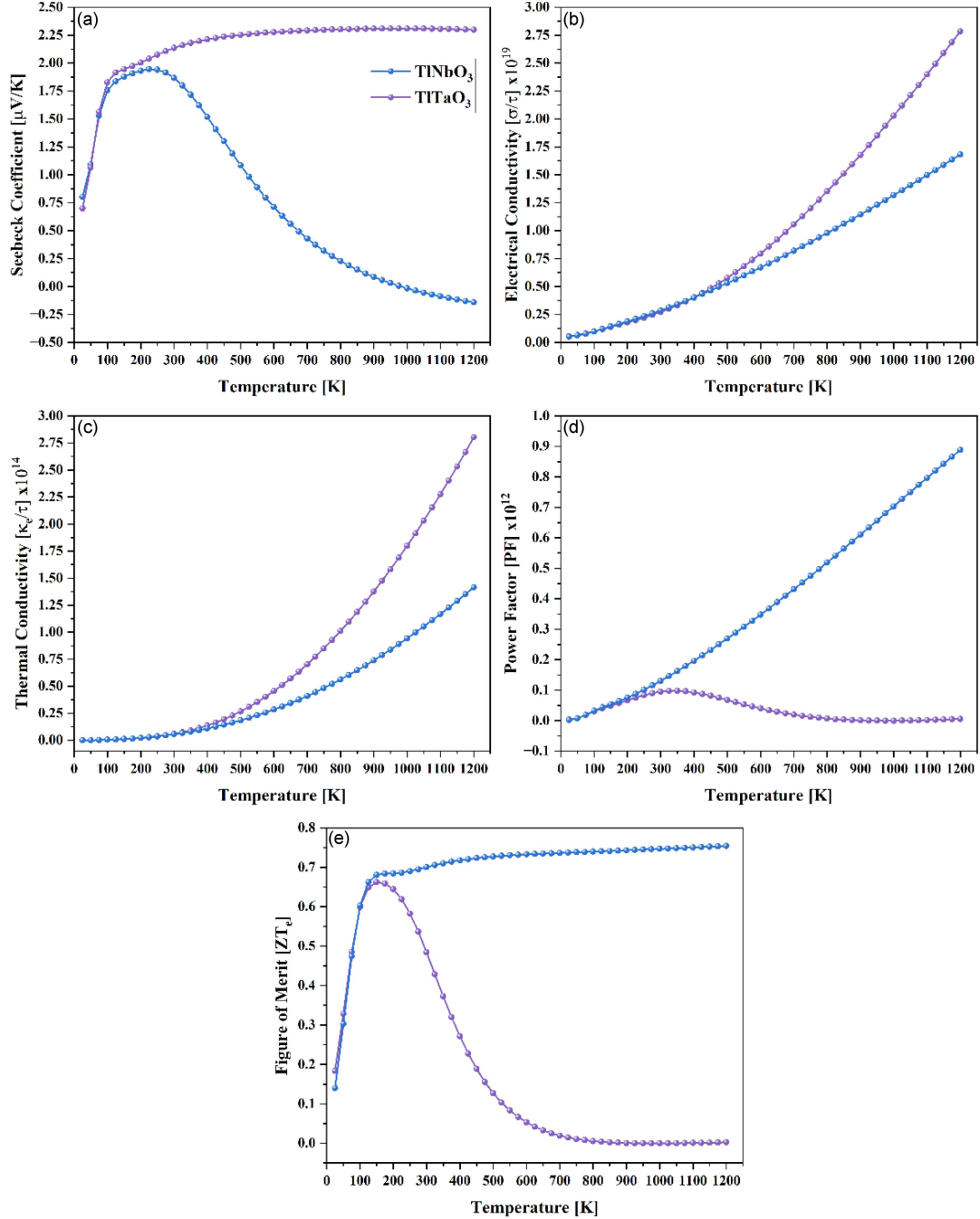


Fig. 10. Comprehensive analysis of thermoelectric properties and performance metrics of TiXO₃ (X = Nb, Ta) perovskite oxides across the temperature range.

varies with temperature for TiTaO₃ and TiNbO₃. As shown in Fig. 10c, both materials demonstrate a substantial increase in thermal conductivity with rising temperature. At low temperatures, TiTaO₃ and TiNbO₃ have relatively modest thermal conductivity values. However, as the temperature increases, both materials exhibit marked improvements in their ability to conduct heat. For example, at 300 K, TiTaO₃ has a thermal conductivity of $\approx 5.59 \times 10^{13}$ W/(m K), while TiNbO₃ shows a slightly higher value

of around 5.89×10^{13} W/(m K). As the temperature approaches 1200 K, the thermal conductivity values rise dramatically, reaching about 1.41×10^{15} W/(m K) for TiTaO₃ and $\approx 2.80 \times 10^{15}$ W/(m K) for TiNbO₃. This significant increase indicates that both materials can efficiently transport heat at elevated temperatures. The greater thermal conductivity of TiNbO₃ at higher temperatures suggests that it may be more effective in dissipating heat, which could be advantageous in thermoelectric applications

where heat management is crucial. Conversely, the lower thermal conductivity of TlTaO_3 may be beneficial for maintaining a temperature gradient, which is essential for optimizing thermoelectric performance [75].

Next, we analyze the power factor depicted in Fig. 10d. The power factor (PF) is a critical parameter in assessing the efficiency of thermoelectric materials, calculated as the product of the square of the Seebeck coefficient and electrical conductivity. This factor plays a significant role in determining the overall thermoelectric performance, contributing to the figure of merit (ZT). From the plotted data, we observe a clear trend, namely, both TlTaO_3 and TlNbO_3 show an increase in power factor with rising temperature. At 25 K, TlTaO_3 has a power factor of $\approx 2.49 \times 10^9 \text{ W}/(\text{m K}^2)$, while TlNbO_3 starts higher, at around $3.48 \times 10^9 \text{ W}/(\text{m K}^2)$. This initial difference suggests that TlNbO_3 has a better ability to convert thermal energy into electrical energy at lower temperatures. As the temperature increases, both materials exhibit significant growth in their power factors. At 300 K, TlTaO_3 reaches a power factor of about $1.31 \times 10^{11} \text{ W}/(\text{m K}^2)$, and TlNbO_3 , despite starting higher, shows a reduction to $\approx 9.50 \times 10^9 \text{ W}/(\text{m K}^2)$. The increasing trend of TlTaO_3 's power factor suggests improved thermoelectric performance as it benefits from higher electrical conductivity and Seebeck coefficient at elevated temperatures. At higher temperatures, particularly approaching 1200 K, TlTaO_3 's power factor continues to rise significantly, reaching around $8.89 \times 10^{11} \text{ W}/(\text{m K}^2)$. In contrast, TlNbO_3 sees a marked decline, with power factor dropping to $\approx 5.53 \times 10^9 \text{ W}/(\text{m K}^2)$, indicating a decrease in its efficiency as a thermoelectric material under these conditions. The divergence in behavior between the two compounds can be attributed to their differing thermal and electrical properties, which influence their capacity to maintain a temperature gradient for efficient energy conversion. The substantial increase in the power factor for TlTaO_3 at higher temperatures positions it favorably for thermoelectric applications, particularly in scenarios requiring efficient heat-to-electricity conversion [76].

Finally, we examine the figure of merit (ZT) presented in Fig. 10e. The figure of merit is a crucial indicator of a material's thermoelectric efficiency, defined as the ratio of the power factor to the product of thermal conductivity and absolute temperature. It reflects how effectively a material can convert heat into electrical energy. From the data plotted, both TlTaO_3 and TlNbO_3 exhibit a general increasing trend in their figure of merit with temperature. At 25 K, TlTaO_3 has a ZT value of ≈ 0.140 , while TlNbO_3 starts higher, at around 0.184. This initial difference highlights TlNbO_3 's relatively superior performance at low temperatures. As the temperature increases, the figure of merit for both materials also rises, reaching values of 0.750 and 0.00237 for TlTaO_3 and TlNbO_3 , respectively, at 1200 K. This

significant increase in ZT for TlTaO_3 illustrates enhanced thermoelectric properties of this material, particularly at higher temperatures, where it becomes more efficient at energy conversion. Throughout the temperature range, TlTaO_3 consistently demonstrates an upward trend in ZT , indicating improvements in either electrical conductivity or Seebeck coefficient of the material or reductions in its thermal conductivity. Conversely, TlNbO_3 shows a slower rate of increase in its figure of merit, suggesting that while it maintains decent performance, it does not improve as significantly as TlTaO_3 under the same thermal conditions. This behavior indicates that TlTaO_3 is a more promising candidate for thermoelectric applications, particularly in high-temperature settings, due to its greater ability to maintain a favorable ZT . The sustained increase in ZT for TlTaO_3 makes it advantageous for applications requiring efficient thermoelectric conversion, while TlNbO_3 , despite starting strong, appears less competitive as temperature rises [70, 71].

4. Conclusions

In conclusion, our study employing GGA-PBE and TB-mBJ potentials within the DFT framework using the WIEN2k code has successfully elucidated the structural, electronic, mechanical, optical, and thermoelectric characteristics of the perovskite oxides TlNbO_3 and TlTaO_3 . Both compounds demonstrate non-magnetic cubic stability, supported by favorable formation energies and phonon dispersion analyses that confirm their dynamic stability. The direct band gaps of 0.17 eV for TlNbO_3 and 1.52 eV for TlTaO_3 reveal the potential of these materials for optoelectronic applications, with density of states analysis indicating significant contributions from Tl, O, and Nb/Ta in the valence and conduction bands. The mechanical stability, as inferred from the various calculated Born parameters, further underscores the robustness of these compounds. Our comprehensive investigation into their optical properties, spanning dielectric functions, reflectivity, refractive index, and absorption coefficients, highlights their suitability for optoelectronic device applications. Additionally, thermoelectric properties analyzed via classical Boltzmann theory reveal a κ/σ ratio of the order of 10^{-5} , indicating low thermal conductivity paired with appreciable electrical conductivity, suggesting excellent thermoelectric performance of these compounds. Notably, the substantial power factor values for TlTaO_3 position it as a promising candidate for thermal applications, paving the way for further exploration of these materials in advanced technologies.

The data that support the findings of this study are available from the corresponding author.

References

- [1] D.P. van Vuuren, N. Nakicenovic, K. Riahi, A. Brew-Hammond, D. Kammen, V. Modi, M. Nilsson, K.R. Smith, *Curr. Opin. Environ. Sustain.* **4**, 18 (2012).
- [2] A. Kalair, N. Abas, M.S. Saleem, A.R. Kalair, N. Khan, *Energy Storage* **3**, e135, (2021).
- [3] A. A. Bazmi and G. Zahedi, "Sustainable energy systems: Role of optimization modeling techniques in power generation and supply—A review," *Renew. Sustain. Energy Rev.* **15**, 3480 (2011).
- [4] A. Tiwari, S. Valyukh, Eds., *Advanced Energy Materials*, 1st ed. Wiley, 2014.
- [5] Q. Li, F.-Z. Yao, Y. Liu, G. Zhang, H. Wang, Q. Wang, *Annu. Rev. Mater. Res.* **48**, 219 (2018).
- [6] H. Liu, H. Fu, L. Sun, C. Lee, E. M. Yeatman, *Renew. Sustain. Energy Rev.* **137**, 110473 (2021).
- [7] M. Xiao, Y. Zhang, J. You, Z. Wang, J.-H. Yun, M. Konarova, G. Liu, L. Wang, *J. Phys. Energy* **4**, 042005 (2022).
- [8] M.E. Calvo, *J. Mater. Chem. A* **5**, 20561 (2017).
- [9] S. Aftab, T. Nawaz, M.B. Tahir, *Int. J. Energy Res.* **45**, 20545 (2021).
- [10] P. Goel, S. Sundriyal, V. Shrivastav, S. Mishra, D.P. Dubal, K.-H. Kim, A. Deep, *Nano Energy* **80**, 105552 (2021).
- [11] Y. Choi, S. Han, B.-I. Park et al., *Nano Converg.* **11**, 36 (2024).
- [12] S. Hussain, M.M. Shahid, *Green Energy Environ. Technol.* **3**, 1 (2024).
- [13] S. Brittman, G.W.P. Adhyaksa, E.C. Garnett, *MRS Commun.* **5**, 7 (2015).
- [14] Y. Gu, Q. Wang, W. Hu, W. Liu, Z. Zhang, F. Pan C. Song, *J. Phys. D Appl. Phys.* **55**, 233001 (2022).
- [15] G. Koster, L. Klein, W. Siemons, G. Rijnders, J.S. Dodge, C.-B. Eom, D.H.A. Blank, M.R. Beasley, *Rev. Mod. Phys.* **84**, 253 (2012).
- [16] A. Jain, Y.G. Wang, L.N. Shi, *J. Alloys Compd.* **928**, 167066 (2022).
- [17] J. Gao, D. Xue, W. Liu, C. Zhou, X. Ren, *Actuators* **6**, 24 (2017).
- [18] M. Acosta, N. Novak, V. Rojas, S. Patel, R. Vaish, J. Koruza, G.A. Rossetti Jr., J. Rödel, *Appl. Phys. Rev.* **4**, 041305 (2017).
- [19] J. Qian, B. Xu, W. Tian, *Org. Electron.* **37**, 61 (2016).
- [20] R. Lu, Y. Liu, J. Zhang, D. Zhao, X. Guo, C. Li, *Chem. Eng. J.* **433**, 133845 (2022).
- [21] A.Y. Alsalloum, B. Turedi, X. Zheng et al., *ACS Energy Lett.* **5**, 657 (2020).
- [22] P. Sharma, P. Ranjan, T. Chakraborty, *Chem. Phys. Impact* **7**, 100344 (2023).
- [23] S.U. Zaman, S. Khan, N. Mehmood, A.U. Rahman, R. Ahmad, N. Sultan, F. Ullah, H.J. Kim, *Opt. Quant. Electron.* **54**, 396 (2022).
- [24] D.R. Onken, D. Perrodin, S.C. Vogel, E.D. Bourret, F. Moretti, *Acta Crystallogr. E Cryst. Commun.* **76**, 1716 (2020).
- [25] Q.V. Phan, H.J. Kim, G. Rooh, S.H. Kim, *J. Alloys Compd.* **766**, 326 (2018).
- [26] R. Hawrami, E. Ariesanti, V. Buliga, A. Burger, S. Lam, S. Motakef, *J. Cryst. Growth* **531**, 125316 (2020).
- [27] S.U. Zaman, N. Rahman, M. Arif, M. Saqib, M. Husain, E. Bonyah, Z. Shah, S. Zulfiqar, A. Khan, *AIP Adv.* **11**, 015204 (2021).
- [28] H.P. Beck, M. Schramm, R. Haberkorn, *J. Solid State Chem.* **146**, 351 (1999).
- [29] D.J. Singh, *J. Appl. Phys.* **112**, 083509 (2012).
- [30] S. Sharma, N. Weiden, A. Weiss, *Z. Naturforsch. A* **42**, 1313 (1987).
- [31] R. Yadav, A. Srivastava, J.A. Abraham, R. Sharma, S.A. Dar, *SSRN J.* **2022**, 1 (2022).
- [32] G. Ayub, A. Rauf, M. Husain et al., *ACS Omega* **8**, 17779 (2023).
- [33] I. Hany, G. Yang, Q.V. Phan, H.J. Kim, *Mater. Sci. Semicond. Process.* **121**, 105392 (2021).
- [34] F. Yousefzadeh, Q.A. Yousif, M. Ghanbari, M. Salavati-Niasari, *J. Mol. Liq.* **349**, 118443 (2022).
- [35] S.K. Mitro, M. Saiduzzaman, K.M. Hossain, J.K. Rony, S. Ahmad, *J. Mater. Res.* **38**, 2007 (2023).
- [36] Y. Jin, J. Li, G. Wang, Q. Zhang, Z. Liu, X. Mao, *Phys. Chem. Chem. Phys.* **24**, 17561 (2022).
- [37] G. Yang, Q. V. Phan, M. Liu, A. Hawari, H. Kim, *Nucl. Instrum. Methods Phys. Res. A* **954**, 161516 (2020).
- [38] W. Hasan, A.M. Hossain, M. Rashe-duzzaman, M.A. Rahman, M.M. Hossain, K.R. Mohammad, R. Chowdhury, K.M. Hossain, M.M. Hossena, M.Z. Hasan, *RSC Adv.* **12**, 27492 (2022).
- [39] M. Petersen, F. Wagner, L. Hufnagel, M. Scheffler, P. Blaha, K. Schwarz, *Comput. Phys. Commun.* **126**, 294 (2000).

- [40] K. Schwarz, P. Blaha, *Comput. Mater. Sci.* **28**, 259 (2003).
- [41] M. Orio, D.A. Pantazis, F. Neese, *Photosynth. Res.* **102**, 443 (2009).
- [42] P. Hohenberg, W. Kohn, *Phys. Rev.* **136**, B864 (1964).
- [43] J.P. Perdew, K. Burke, M. Ernzerhof, *Phys. Rev. Lett.* **77**, 3865 (1996).
- [44] D. Koller, F. Tran, P. Blaha, *Phys. Rev. B* **83**, 195134 (2011).
- [45] A. Togo, *J. Phys. Soc. Jpn.* **92**, 012001 (2023).
- [46] H.U. Yang, J. D'Archangel, M.L. Sundheimer, E. Tucker, G.D. Boreman, M.B. Raschke, *Phys. Rev. B* **91**, 235137 (2015).
- [47] G.K.H. Madsen, D.J. Singh, *Comput. Phys. Commun.* **175**, 67 (2006).
- [48] M. Liang, W. Lin, Z. Lan, J. Meng, Q. Zhao, X. Zou, I.E. Castelli, T. Pullerits, S.E. Canton, K. Zheng, *ACS Appl. Electron. Mater.* **2**, 1402 (2020).
- [49] S.C. Tidrow, *Ferroelectrics* **470**, 13 (2014).
- [50] H. Cho, Y. Kim, C. Wolf, H. Lee, T. Lee, *Adv. Mater.* **30**, 1704587 (2018).
- [51] V.G. Tyuterev, N. Vast, *Comput. Mater. Sci.* **38**, 350 (2006).
- [52] S. Lakra, S.K. Mukherjee, *J. Comput. Chem.* **45**, 1008 (2024).
- [53] A.A. Emery, C. Wolverton, *Sci. Data* **4**, 170153 (2017).
- [54] C.J. Bartel, A. Trewartha, Q. Wang, A. Dunn, A. Jain, G. Ceder, *npj Comput. Mater.* **6**, 97 (2020).
- [55] G. Hautier, S.P. Ong, A. Jain, C.J. Moore, G. Ceder, *Phys. Rev. B* **85**, 155208 (2012).
- [56] X. Qian, R. Yang, *Phys. Rev. B* **98**, 224108 (2018).
- [57] T. Ma, P. Chakraborty, X. Guo, L. Cao, Y. Wang, *Int. J. Thermophys.* **41**, 9 (2020).
- [58] D.D. Satikunvar, N.K. Bhatt, B.Y. Thakore, *J. Appl. Phys.* **129**, 035107 (2021).
- [59] J. He, D. Hitchcock, I. Bredeson, N. Hickman, T.M. Tritt, S.N. Zhang, *Phys. Rev. B* **81**, 134302 (2010).
- [60] M. Nomura, J. Shiomi, T. Shiga, R. Anufriev, *Jpn. J. Appl. Phys.* **57**, 080101 (2018).
- [61] A.M. Smith S. Nie, *Acc. Chem. Res.* **43**, 190 (2010).
- [62] M. Razeghi, A. Rogalski, *J. Appl. Phys.* **79**, 7433 (1996).
- [63] S. Bouhmaidi, M.B. Uddin, R.K. Pingak, S. Ahmad, M.H.K. Rubel, A. Hakamy, L. Setti, *Mater. Today Commun.* **37**, 107025 (2023).
- [64] S.Q. Wang, H.Q. Ye, *Phys. Status Solidi (b)* **240**, 45 (2003).
- [65] R. Kubo, *Butsuri* **10**, 175 (1955).
- [66] A.S. Verma, A. Kumar, *J. Alloys Compd.* **541**, 210 (2012).
- [67] S.F. Pugh, *Lond. Edinb. Dubl. Phil. Mag. J. Sci.* **45**, 823 (1954).
- [68] M. Braun I. Iváñez, *Extreme Mech. Lett.* **39**, 100821 (2020).
- [69] S. Sahin, Y.O. Ciftci, K. Colakoglu, N. Korozlu, *J. Alloys Compd.* **529**, 1 (2012).
- [70] S.F. Pugh, *Lond. Edinb. Dubl. Phil. Mag. J. Sci.* **45**, 823 (1954).
- [71] H. Niu, X.-Q. Chen, P. Liu, W. Xing, X. Cheng, D. Li, Y. Li, *Sci. Rep.* **2**, 718 (2012).
- [72] B. Lakhdar, B. Anissa, D. Radouan, N. Al Bouzieh, N. Amrane, *Opt. Quant. Electron.* **56**, 313 (2024).
- [73] K. Yamamoto, G. Narita, J. Yamasaki, S. Iikubo, *J. Phys. Chem. Solids* **140**, 109372 (2020).
- [74] S.A. Khandy, D.C. Gupta, *J. Magn. Magn. Mater.* **458**, 176 (2018).
- [75] Q. Mahmood, T. Ghrib, A. Rached, A. Laref, M.A. Kamran, *Mater. Sci. Semi-cond. Process.* **112**, 105009 (2020).
- [76] N.A. Noor, M.W. Iqbal, T. Zelai, A. Mahmood, H.M. Shaikh, S.M. Ramay, W. Al-Masry, *J. Mater. Res. Technol.* **13**, 2491 (2021).